Made available through a Creative Commons CC-BY License

ACS APPLIED MATERIALS & INTERFACES

www.acsami.org

Research Article

Heterostructured $TiO_2/SiO_2/\gamma\text{-}Fe_2O_3$/rGO Coating with Highly Efficient Visible-Light-Induced Self-Cleaning Properties for Metallic Artifacts

Maryam Mokhtarifar, Reyhaneh Kaveh, Mojtaba Bagherzadeh, Andrea Lucotti, MariaPia Pedeferri, and Maria Vittoria Diamanti*

Cite This: *ACS Appl. Mater. Interfaces* 2020, 12, 29671−29683

Read Online

ACCESS | Metrics & More | Article Recommendations | Supporting Information

ABSTRACT: A novel nanohybrid composite of TiO_2, SiO_2, γ-Fe_2O_3, and reduced graphene oxide (TiO_2@Si:Fe:rGO) is fabricated by the sol−gel method. The properties of the coated film were examined by structural and self-cleaning analyses using simulated discoloration/soiling and roofing tests. The fabricated transparent TiO_2@Si:Fe:rGO composite showed excellent photoactivity and wettability, behaving well in self-cleaning applications. The addition of SiO_2 improved the crystalline structure and surface hydroxylation of TiO_2 nanoparticles. γ-Fe_2O_3 decreased the recombination rate of e^-/h^+ pairs, and significantly improved photocatalytic activity under visible light. Moreover, rGO sheets as excellent electron acceptors and transporters also reduced recombination, as well as affected wettability, achieving superhydrophilicity under irradiation. The coated substrate showed excellent resistance to simulated acid rain and significantly preserved the substrate from soiling in roofing tests.

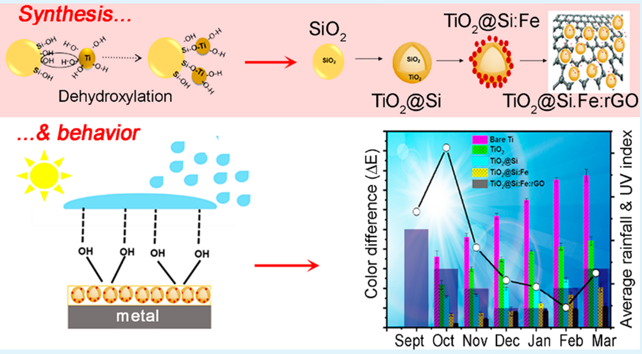

KEYWORDS: *self-cleaning, TiO_2, γ-Fe_2O_3, SiO_2, reduced graphene oxide, superhydrophilic photocatalyst, transparent coating*

Downloaded via POLITECNICO DI MILANO on June 15, 2022 at 11:47:51 (UTC).
See https://pubs.acs.org/sharingguidelines for options on how to legitimately share published articles.

1. INTRODUCTION

Preservation of current and future artifacts that have left a valuable visual art legacy is of great importance in today's world. However, atmospheric deterioration continues to threaten tangible architectural heritages, especially those buildings and monuments made out of metals that are highly prone to various types of outdoor declines, including degradation and discoloration.[1−5]

To overcome this challenge, many studies have been dedicated to the elimination of pollutants by using photoactive metal oxides such as WO_3, ZnO, and TiO_2.[6−9] Among them, TiO_2 is one of the most considerable materials in the built environment due to its high photocatalytic efficiency and good integration with building materials. Indeed, its physicochemical properties, such as high chemical stability, easy availability, and the possibility to be easily added as coating or in mass to cementitious materials or to be deposited in the form of a thin film and reaching the superhydrophilic state, make it a great candidate for the preservation of metallic artifacts. The effect is that of reducing maintenance time and cost and protecting them from soiling by means of its self-cleaning features.[9−13] Besides, some of the general aspects of suitable coatings to preserve metallic historic and modern buildings exposed to harsh environmental situations are proper adhesion, chemical stability, colorlessness, and transparency to maintain the aesthetic characteristics of the original material.[14]

To furtherly increase the photocatalytic efficiency, it is essential to engineer TiO_2 hydrophilic surfaces to maximize the removal of contaminants and counteract soiling and discoloration. However, the wide band gap of the semiconductor for both anatase and rutile forms of TiO_2 limits both its hydrophilic conversion and photocatalytic activity and, consequently, its self-cleaning ability to happen only at 5% of the solar spectrum, i.e., the UV region of sunlight.[15]

Within this context, heterojunction structures that combine other narrow band gap metal oxides with TiO_2 can be used to achieve better light-harvesting and charge transport properties. On the other hand, the presence of the metal oxides in TiO_2 composites could promote the electron transfer reactions between the photocatalyst and pollutant molecules. Moreover, materials with high specific surface area such as carbon-based

Received: April 13, 2020
Accepted: June 3, 2020
Published: June 3, 2020

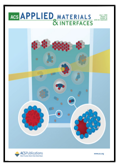

© 2020 American Chemical Society

https://dx.doi.org/10.1021/acsami.0c06792

materials can be utilized as an excellent supporting material to amplify photoactivity by increasing available surface sites.[16,17]

Trying to face this challenge, the present work aims at the synthesis and characterization of a nanocomposite coating including silicon dioxide (SiO_2), γ-iron oxide (γ-Fe_2O_3), and reduced graphene oxide (rGO)) on titanium substrates. The synergistic effects of the components above with TiO_2 are investigated in terms of resulting film morphological, structural and functional characteristics with special reference to self-cleaning practical applications.

2. MATERIALS AND METHODS

2.1. Preparation of Sols and Coatings. Iron chloride tetrahydrate ($FeCl_2$. $4H_2O$), propylene oxide, tetraethyl orthosilicate (TEOS), tetrabutyl titanate (TBT), sulfuric acid (H_2SO_4), graphene oxide solution (GO), sodium borohydride ($NaBH_4$), ethanol (C_2H_5OH), and methylene blue (MB) were purchased from Sigma−Aldrich and used as received. To prepare the γ-Fe_2O_3 nanoparticles, $FeCl_2 \cdot H_2O$ (5 mmol) was dissolved in ethanol (0.3 M) and then added to propylene oxide (50 mmol), sonicated for 15 min, and followed by stirring for 6 h. Then, the resulting solution was heated at around 100 °C to obtain a brown powder.

To synthesize rGO, $NaBH_4$ (6 mmol) was dissolved in diluted water (0.3 M) and then the solution was sonicated for 10 min. The aqueous solution was added dropwise to 5 mL of homogeneous GO aqueous dispersion (2 mg/mL), while it was being stirred at 80 °C for 1 h. The suspension was centrifuged and washed several times to obtain a black powder of rGO.

A homogeneous TiO_2@Si:Fe:rGO sol−gel was synthesized by adding TEOS (40 mmol) to 65% HNO_3 and stirring the solution for 1 h (the molar ratio of TEOS and H^+ was kept 2.4) followed by centrifuging and drying at room temperature for 10 h. The obtained powder was dissolved in 10 mL of ethanol under sonification for 1 h, and then propylene oxide (400 mmol) and TBT (40 mmol) were added to the solution to form solution A that was then aged for 72 h. Solution A was mixed with 0.032 g of as prepared γ-Fe_2O_3 nanoparticles, and the mixture was sonicated for 1 h to obtain solution B. Finally, 0.02 g of the obtained rGO powder and solution B were mixed via stirring for 2 h and the obtained solution was named as TiO_2@Si:Fe:rGO (for some comparison, a solution including just TiO_2 was prepared as well). The concentration of TiO_2 and SiO_2 components followed the work of Kwon et al.[18]

Supporting Information Figure S1 shows a schematic representation of the TiO_2@Si:Fe:rGO synthesis. In this figure, it can be observed that the SiO_2 and TiO_2 particles are bound by -Si−O−Ti- bonds. The strength of the chemical bond is stronger than that of van der Waals forces and other physical forces, so the coating of nano-TiO_2 on a SiO_2 surface is stable.[19] The TiO_2@Si:Fe nanoparticles then lie on the sheets of rGO.[20,21]

The final sol produced, TiO_2@Si:Fe:rGO and the intermediate sols TiO_2, TiO_2@Si, and TiO_2@Si:Fe were then applied to metallic substrates, consisting of commercial purity titanium specimens, grade 2 ASTM, with dimensions 50 mm × 50 mm and thickness 0.5 mm. All specimens were coated in the TiO_2@Si:Fe:rGO sol with the dip-coating method. Although spray coating could be more applicable in the field of cultural heritage preservation as well as building materials functionalization, dip coating was selected in this work in order to have a better control on the process, resulting an uniform thickness and morphology.[22−24] These properties could be adjusted with changing some parameters such as immersion/withdrawal speeds, angle, and number of dip coatings.[25−29] However, because the solution is watery, it could be easily applied with spray-coating technique as well.

The number of dips was always set to be two, and the immersion rate was kept at 200 mm/min while the withdrawal rate was modulated at 100 mm/min. Careful consideration was taken into account for setting the bottom edge of the substrate to the solution surface, as well as dipping angles (90°). To have coated substrates with the same geometric area, a selected area of 1.7 × 1.9 cm^2 was exposed and the rest of the sample was covered with Kapton tape. The process was done with a drying phase in ambient conditions for 24 h between each dipping followed by calcination at 600 °C for 2 h.

2.2. Characterization. All of the materials were characterized using field emission scanning electron microscopy (FE-SEM), X-ray fluorescence (XRF), X-ray diffraction (XRD), Raman spectroscopy, Fourier transform infrared (FTIR) spectroscopy, atomic force microscopy (AFM), UV−vis−near-IR diffuse reflectance spectroscopy, and optical microscopy (OM) to understand their structure, optical properties, photocatalytic performances, and the stabilities of the coated films.

The morphologies of the powder samples (TiO_2@Si and TiO_2@Si:Fe:rGO) were evaluated by FESEM (TESCANMIRA II). For samples preparation, the synthesized nanoparticles were dispersed in ethanol and then a drop of mixed solution was withdrawn and dried on an aluminum plate. XRD was used to investigate the crystalline structures in the coated samples; diffraction patterns were recorded on a Philips PW1830 powder diffractometer operating at 40 kV voltage and 40 mA filament current. Spectra were acquired at the scanning rate of 2.5 deg/min with Cu Kα_1 radiation in the 2θ range 20−60°. The weight fractions of anatase and rutile were calculated according to eq 1,[30] where I_R and I_A are the intensity of the strongest reflections for rutile and anatase in (110) and (101) phases, individually.

$$f_A/\% = \frac{1}{\left(1 + 1.26\frac{(I_R)}{(I_A)}\right)} \tag{1}$$

For the composition analysis XRF was employed (ARL PERFORM'X). The optical properties were investigated by UV−vis−near-IR diffuse reflectance spectra, recorded in the 220−2600 nm range with a Shimadzu UV 3600 Plus spectrophotometer equipped with an ISR-603 integrating sphere, and $BaSO_4$ was used as the reference material. The band gap was calculated on the basis of the reflectance UV−vis spectra after Kubelka−Munk conversion using the Tauc plot method.[31] The FT-IR spectra of the prepared samples were recorded on a Bruker Tensor 27 spectrometer using a KBr pellet for sample preparation at room temperature. The Raman spectra were measured with a LABRAM HR800 equipped with a Peltier cooled CCD detector, and λ = 514 nm excitation was done by an argon ion laser (Stabilite 2017, Spectra-Physics). The laser radiation was filtered by an interference filter and focused on the sample by an Olympus BX41 microscope. A 50× Olympus objective with a 0.7 numerical aperture was utilized. The Rayleigh radiation was rejected using Notch filters for the λ = 514 nm laser line. Surface roughness of the coated samples was studied by atomic force microscopy (AFM) using a NT-MDT AFM Solver Pro apparatus operating in contact mode on an area of 60 μm × 60 μm. The coated samples were deposited on titanium specimens with an initial mirror polish surface finish to allow the investigation of the roughness associated with the composite deposition. Optical microscopy (OM) was used to assess possible cracking of the film before and after photodegradation test, in order to give a first evaluation of film structural stability (Leica INM 200). In addition, adhesion was evaluated by comparing OM images before and after making a scratched line at the coated samples using a diamond tip.

To evaluate self-cleaning properties, the wettability of the coated thin films was examined from the contact angle (CA) of a water droplet. These measurements were done on five predefined positions by a CCD camera connected to the computer via a PCI card. For each sample, the average contact angle was measured both under dark and after illumination for 30 min. Measurements were repeated after discoloration tests to check whether the coatings maintained their self-cleaning attitude also after possible discoloration.

2.3. Photocatalytic Degradation Performance. The photocatalytic activity of the coated thin films was characterized in methylene blue degradation under UV and visible light irradiation by spectrophotometry (UV−vis spectrophotometer, Thermo Scientific

Table 1. Volume Fractions of Soiling Mixtures Used to Mimic the Soiling of Roofing Materials

site	artifact	soiling components (%) carbon black	humic acid	dust	salt
Cleveland, OH, USA	Peter B. Lewis building	8	0	61	31
Glasgow, United Kingdom	Glasgow Science Centre	6	15	52	27
Normandy, France	Juno Beach Centre	12	36	28	24
Patras, Greece	Patras museum	5	8	63	24

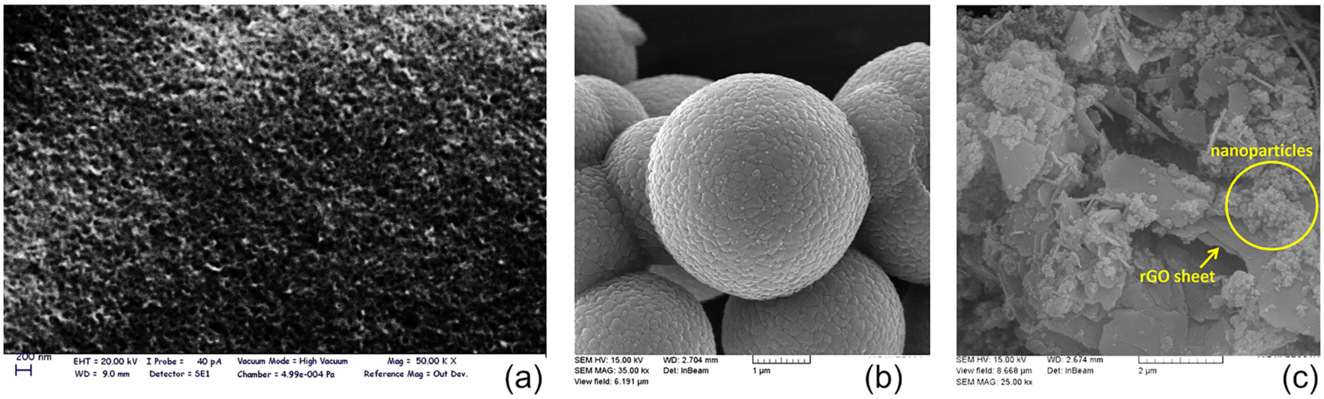

Figure 1. SEM images of (a) structure of TiO_2@Si:Fe:rGO thin film, (b, c) distribution of the nanoparticles in TiO_2@Si and TiO_2@Si:Fe:rGO composites, respectively.

Spectronic 200E) at the wavelength 668 nm where MB has its maximum absorbance.

In a typical experiment, the MB solution was prepared by adding dye to deionized water (10^{-5} M), and then the coated specimens (1.7 × 1.9 cm^2) were put in the MB solution (40 mL). Before photodegradation, the specimens were kept in the dark for 50 min to reach adsorption−desorption equilibrium. The samples were then illuminated for 6 h under UV LED (500 mA, 3.8 V) and visible LED (700 mA, 3 V) with 3 cm LED−sample distance. Eventually, the photodegradation of MB was calculated as a function of the relative MB concentration versus time of reaction, C/C_o, where C_o is the initial concentration of MB solution and C is the concentration at sampling time, as derived from absorption values. Pseudo-first-order kinetics was hypothesized to control the rate of MB photodegradation, as observed in related scientific literature,[32,33] so the slope of the curve of $\ln(C/C_o)$ versus time of reaction was taken as MB photodegradation rate constant k.

2.4. Simulated Artificial Soiling. The typical composition of soiling present on urban surfaces is mostly including four soiling agents that were selected in this experimental work to mimic natural soiling: black carbon, mineral dust, humic acids (organics), and inorganic salts. The four soiling agents were mixed in different ratios in an aqueous mixture and applied to the samples' surfaces. Dip deposition of the soiling agents with 45° dipping angle was chosen for ease of control and because soot deposition is typically waterborne.[34] These individual components were selected to simulate soiling of metallic roofings exposed in four different climates representative of different cites with modern and contemporary titanium-based artifacts that have varying polluted atmospheres[35,36] (Figure S2 and Table 1).

To study the self-cleaning ability of the coated titanium specimens, they were put under solar light for 1 h to be photoactived and then dipped in the soiling components immediately. The soiled plates were left to dry; then the change in their color due to soiling was measured by a portable spectrophotometer Konica Minolta 2500d working in reflectance mode and compared with their initial color.

Roofing test measurements were taken from September to March 2019, in Milan, Italy. The samples were exposed outdoors by fixing them on a rack that was placed on the roof of a building, 45° tilt angle, facing South. The colors of specimens were monitored for 6 months at the beginning of each month.

Color changes before and after the tests were evaluated in terms of color difference, according to the $L^*a^*b^*$ color system: $\Delta E = \sqrt{((\Delta L^*)^2 + (\Delta a^*)^2 + (\Delta b^*)^2)}$; the larger the color difference ΔE, the more significant was the discoloration. Here, symbols ΔL^*, Δa^*, and Δb^* refer to the differences in L^*, a^*, and b^* values, respectively, of the samples before and after tests.

2.5. Simulated Acid Rain Test. Metals freshly exposed to atmosphere as building roofs and walls are immune to pitting or crevice corrosion; nevertheless, these metals may undergo color changing after prolonged exposure. In the case of titanium, discoloration is a result of the formation of oxide films on the surface, which show interference colors by interacting with light.[4,37,38] It is proved that discoloration is accelerated in the presence of titanium carbide (TiC) on the titanium surface, which is introduced in the sheet during the manufacturing process.[39] Even though color changing does not adversely affect the structural function of the metal components, it sometimes spoils the building appearance.[40,41] Furthermore, it is proved that the rate of discoloration changed depending on the building location and material factors, even though different sheets were adjacent to each other on the same building.[40]

To evaluate discoloration resistance of the samples, bare and coated titanium pieces were immersed in solutions of prescribed pH values simulating acid rain, obtained by adding H_2SO_4 and NaOH to distilled water. Other environmental factors such as air-borne salts and ultraviolet rays are not investigated here because they were found to have a marginal effect on metals discoloration.[37] The solution pH for the immersion tests was controlled in a range of 3−7 by changing the ratio of sulfuric acid and sodium hydroxide, and the specimens were immersed in the solution kept at 65 °C for 7 days to accelerate the procedure.

3. RESULTS AND DISCUSSION

3.1. Structure of the Coated Films. FESEM morphology images of synthesized composites are reported in Figure 1. On the basis of Figure 1a, TiO_2@Si:Fe:rGO thin film shows apparently a uniform coating structure though more detail on particles distribution could be figured out from powder SEM morphology. Hence, images of the TiO_2@Si and TiO_2@Si:Fe:rGO composite powders are presented in Figure 1a,b, respectively.

https://dx.doi.org/10.1021/acsami.0c06792
ACS Appl. Mater. Interfaces 2020, 12, 29671−29683

Table 2. XRF Analysis Results of the TiO_2@Si:Fe:rGO Sample

sample	TiO_2	SiO_2	Fe_2O_3	Na_2O	Al_2O_3	K_2O	MnO	P_2O_5	LOI
analysis (%)	38.79	34.85	0.915	0.1	0.09	0.07	0.01	0.009	25.127

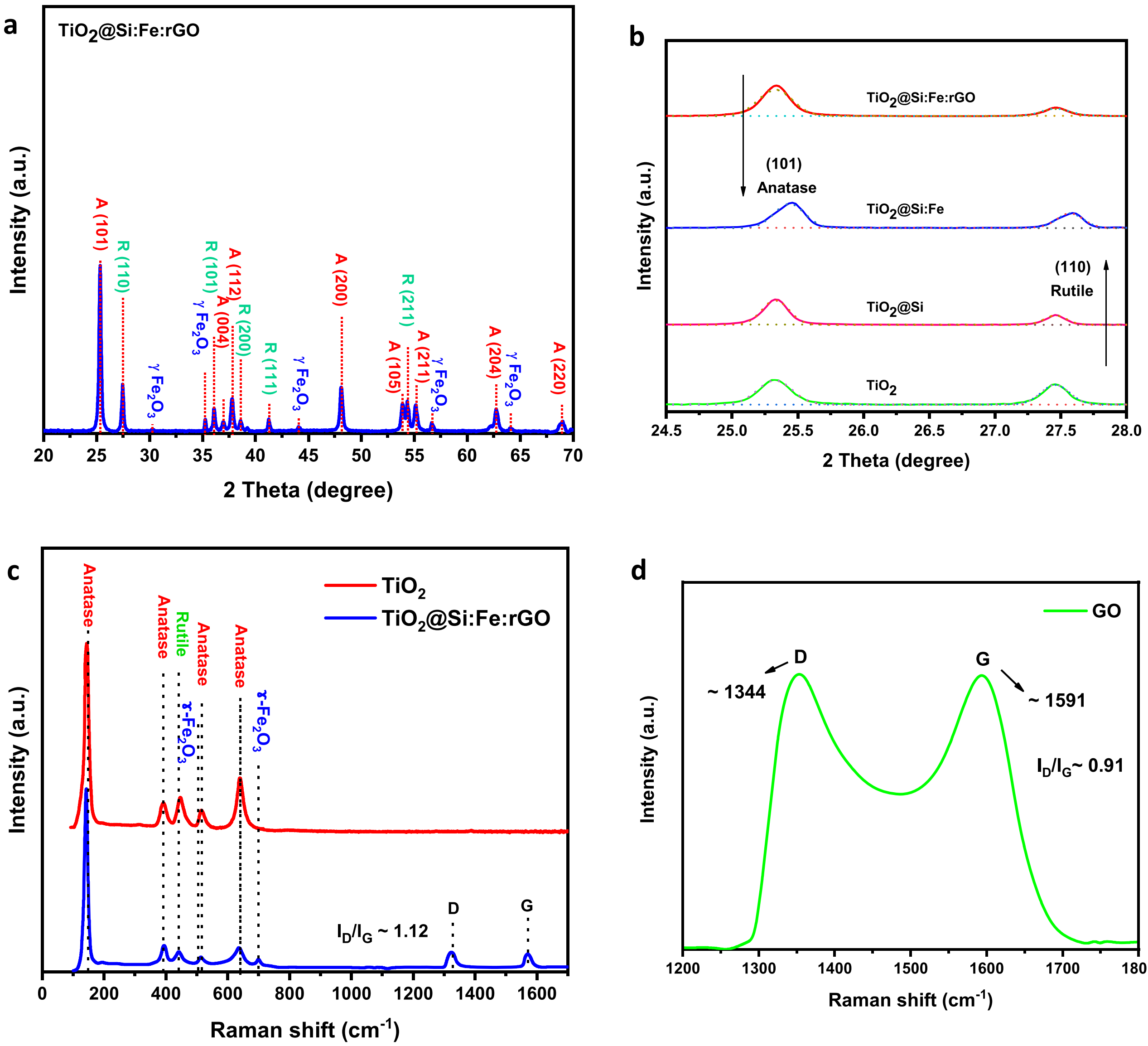

Figure 2. XRD patterns of (a) TiO_2@Si:Fe:rGO coated film and (b) anatase (101) and rutile (110) peaks of the samples after heat treatment at 600 °C. Raman spectra of (c) TiO_2 and TiO_2@Si:Fe:rGO and (d) GO samples in the wavenumber range from 100 to 1800 cm^{-1}.

Figure 1b reveals that TiO_2 nanoparticles have smaller diameter and are dispersed on SiO_2 particle surfaces uniformly. In panel c, it could be observed that particles of TiO_2, SiO_2 and γ-Fe_2O_3 are well distributed on the surface of the rGO nanosheets and well served as substrate for the homogeneous distribution of the nanoparticles.

XRF analysis results are presented in Table 2. This table shows the chemical compositions in the sample of TiO_2@Si:Fe:rGO.

According to the obtained results, the atomic ratios Ti/Si and Ti/Fe were calculated as 0.83 and 44, respectively.

XRD patterns and crystalline structures of the coated samples calcined at 600 °C are presented in Figure 2a,b and Table 3, respectively. It can be observed that the addition of SiO_2 to TiO_2 enhanced the thermal stability of anatase TiO_2 crystallites, resulting in the retardation of the anatase-to-rutile phase transition. Indeed, the presence of SiO_2 can prevent the nucleation of rutile.[42] No peak for silica was observed; hence, SiO_2 is amorphous. Crystallite sizes obtained by Scherrer

Table 3. Anatase Percentage in Crystalline TiO_2 (Calculated by Spurr Equation) and Anatase Particle Size (Calculated by Scherrer Equation)

			particle size (nm)	
sample	anatase (%)	rutile (%)	anatase	rutile
TiO_2	54	46	31	40
TiO_2@Si	64	36	28	42
TiO_2@Si:Fe	59	41	24	36
TiO_2@Si:Fe:rGO	71	29	23	33

equation were about 31 and 27 nm for the samples of TiO_2 and TiO_2@Si calcined at 600 °C, respectively. From literature it is known that for this transition to occur, anatase particles need to grow to a sufficient size, anatase being thermodynamically more stable for small nanoparticles. However, the contribution of bulk energy to total energy increases along with particle size. The transition to rutile takes place in a reconstructive process to decrease the total energy. In this way, the presence of SiO_2 prevented phase transition by inhibiting the growth of the primary particles. The presence of SiO_2 around TiO_2 could efficiently delay the growth of nanoparticles likely due to the formation of the Ti−O−Si bond and because of the presence of amorphous SiO_2 in contact with TiO_2, which would hinder the growth of particles of TiO_2.[43−45]

In the TiO_2@Si:Fe composite, since the ionic radius of Fe^{3+} (0.64 Å) is similar to the ionic radius of Ti^{4+} (0.68 Å), the replacement of iron in the matrix of titania is not only possible but also favorable.[46] Thus, structural deformations and the presence of defects in the TiO_2 crystals might have formed by the substitution of Ti^{4+} by Fe^{3+}, which marginally reduces the crystallinity of TiO_2.[47] In the presence of Fe_2O_3 in the TiO_2@Si:Fe composite, anatase TiO_2 peaks decrease in intensity while peaks for rutile phase start appearing. This observation indicates that Fe(III) ions have substantial influence on the anatase titania phase in binary TiO_2−Fe_2O_3 compounds. The incorporation of Fe_2O_3 in the titania matrix might have facilitated the anatase−rutile phase transformation, indicating the presence of Fe^{3+} ions as substitutes in titania crystals.[46−51]

Also, the XRD pattern of this sample shows diffraction peaks corresponding to the (220), (311), (400), (511), and (440) planes of γ-Fe_2O_3 (Figure 2b)[52] but no separate peak for rGO in the composite, possibly due to the low amount and low intensity of rGO. Moreover, the characteristic peak of rGO at 24.5° may be screened by the main peak of anatase TiO_2 at 25.3°.[50]

Interestingly, TiO_2 phase transformation from anatase to rutile was retarded, as the anatase/rutile ratio increased by adding rGO in the sol; hence, the presence of carbon retarded the anatase-to-rutile transformation, as already reported in literature related to activated carbon.[50] This may be attributed to the high surface area of rGO, as well as to a reduction of acidity and promotion of the dehydration of Ti^{4+} complex, by forming edge shared bonds, thus producing anatase phase by adding rGO in the nanocomposite.[51,53] Indeed, a variation in the number of OH ligands in the Ti complex produced from Ti^{4+} hydrolysis was observed to change acidity.[52,54,55]

Crystallographic structures of the prepared samples were also investigated by Raman spectroscopy and exhibited in Figure 2c,d. Scatterings at 145, 393, and 638 cm^{-1} are characteristic of anatase, while the one at 445 cm^{-1} is related to rutile.[42] Given a smaller crystallite size and consequent relaxation of surface atoms, which are lacking adjacent atoms, peaks are slightly shifted in TiO_2@Si:Fe:rGO.[48] For this sample both characteristic bands of D and G peaks of GO, located at 1323 and 1570 cm^{-1}, have shifted to lower frequencies in comparison with pure GO. This issue can be good evidence that GO was successfully reduced. Also, the intensity of I_D/I_G ratio peaks of TiO_2@Si:Fe:rGO compared to pure GO was enhanced. It can be related to the reduced average size of sp^2 domains during the reduction process of GO in TiO_2@Si:Fe:rGO nanocomposite. Moreover, peaks at 513 and 700 cm^{-1} were attributed to the presence of γ-Fe_2O_3 in this nanocomposite.[56]

The FT-IR spectra of the TiO_2, TiO_2@Si, γ-Fe_2O_3, and TiO_2@Si:Fe:rGO samples is shown in the wavenumber range from 300 to 4000 cm^{-1} (Figure 3). TiO_2 shows three bands including a broad absorption band at around 3500 cm^{-1}, related to the stretching vibration of hydroxyl groups O−H bound to the surface of TiO_2, an absorption band at 1627 cm^{-1}, due to bending of Ti−OH, and an absorption band at 1381 cm^{-1} for Ti−O modes. In TiO_2@Si, at ∼970 cm^{-1} Ti−O−Si bonds appear, which are responsible for delayed anatase-to-rutile transformation (see XRD results).[57,58] Moreover, the absorption band at 1104 cm^{-1} is attributed to the asymmetric Si−O−Si stretching vibration. γ-Fe_2O_3 shows strong bands at 453 and 544 cm^{-1} (Fe−O groups); these peaks were shifted to 448 and 538 cm^{-1} in TiO_2@Si:Fe:rGO probably due to surface augmentation.[59] Eventually, in TiO_2@Si:Fe:rGO, the absorption peak at 1542 cm^{-1} could be related to the skeletal vibration of graphene.[60,61]

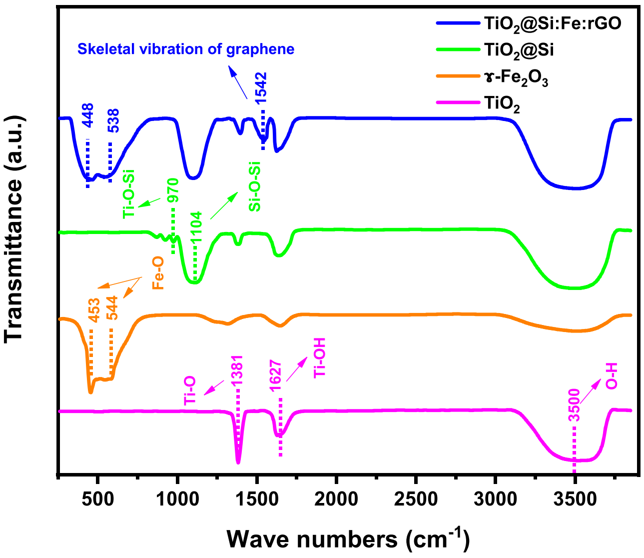

Figure 3. FT-IR spectra of TiO_2, TiO_2@Si, γ-Fe_2O_3, and TiO_2@Si:Fe:rGO samples in the wavenumber range from 300 to 4000 cm^{-1}.

3.2. Roughness and Transmittance.

Figure 4 shows the surface topography of the coated films investigated by AFM. The AFM results imply that the average roughness (R_a) of the

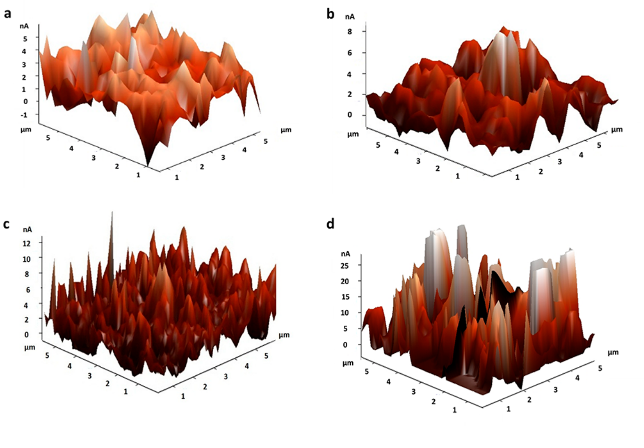

Figure 4. AFM images of (a) TiO_2, (b) TiO_2@Si, (c) TiO_2@Si:Fe, and (d) TiO_2@Si:Fe:rGO coated thin films.

films coated with TiO_2, TiO_2@Si, TiO_2@Si:Fe, and TiO_2@Si:Fe:rGO are 40, 47, 69, and 200 nm, respectively. As can be seen, R_a has a slight increase with the addition of SiO_2 and γ-Fe_2O_3 and a sharp increase with the addition of rGO.[62,63] This result could be correlated to sloppy stacking of rGO sheets, which results in larger channels around the rGO stacks, compatible with the variation in surface roughness.[64] In other words, the rGO assembled layers in TiO_2@Si:Fe:rGO coating probably are in random order and, therefore, are very rough on the surface.[65]

As highlighted above, only such protective coatings which satisfy the maintaining of the aesthetic appearance of artifacts through a transparent and colorless layer can be acceptable.[1,66] Hence, coatings producing an apparent color difference with the substrate are not appropriate for metal protection from discoloration in modern and ancient artifacts, analogously to pointing already drawn in the case of glass both in the solar cell field and in the built environment.[67]

Transmittance spectra in the range of 300−1000 nm were measured on glass slides coated with the different coating materials. As can be seen in Table 4, all coated layers have high transmittance over the entire visible wavelengths range, higher than 80% also in the case of the most complex TiO_2@Si:Fe:rGO coating. This proves that all coatings have good transparency.

Table 4. L^*, a^*, and b^* Colorimetric Coordinates, Color Change ΔE, and Transmittance for Uncoated and Coated Glasses with TiO_2, TiO_2@Si, TiO_2@Si:Fe, and TiO_2@Si:Fe:rGO Thin Films

	L^*	a^*	b^*	ΔE	Transmittance	Samples appearance
Uncoated glass	82.39	0.61	-9.84	0	97 %	
TiO_2	82.67	0.69	-9.35	0.5	95%	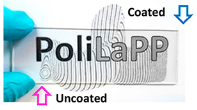
TiO_2@Si	83.47	0.71	-9.17	1.28	93%	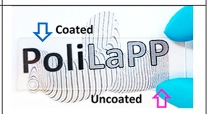
TiO_2@Si:Fe	83.29	1.82	-8.30	2.16	87%	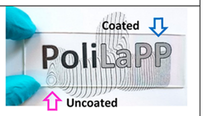
TiO_2@Si:Fe:rGO	83.25	2.01	-7.76	2.65	81%	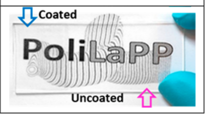

Although transmittance slightly decreased with the addition of SiO_2, γ-Fe_2O_3, and rGO, all samples were still satisfactory from an aesthetic viewpoint. The increased surface roughness could be responsible for the slight loss in optical transmission in the TiO_2@Si:Fe:rGO coating (see Figure 4). Furthermore, TiO_2@Si:Fe film was observed to have a higher absorption intensity than TiO_2@Si (Figure S3). This issue could be a result of electronic interactions between TiO_2@Si and γ-Fe_2O_3 and efficient surface hybridization between these components. Moreover, the TiO_2@Si:Fe:rGO coated film exhibits the highest absorption compared to the other samples, which is expected due to the large optical absorption of both γ-Fe_2O_3 and rGO. None of these coatings generated a color perceivable by naked eyes easily. Spectrophotometric measurements in reflectance mode were performed as well to observe color differences with more details (Table 4). These measurements were done by placing the glass slide on a reference white surface before and after dip coating, to evaluate color changes induced by the application of the coating.

Table 4 also reports the average L^*,a^*,and b^* color coordinates for uncoated and coated samples and the ΔE values calculated using the uncoated sample as reference. In all specimens, the coating induced a slight whitening, observable as a small increase in the luminance parameter (L^*) in TiO_2 and TiO_2@Si. However, L^* decreased again for samples TiO_2@Si:Fe and TiO_2@Si:Fe:rGO, while still higher than uncoated glass. The a^* parameter increased in TiO_2@Si:Fe and TiO_2@Si:Fe:rGO samples as a result of the inherent red color brought about by γ-Fe_2O_3. Also, the b^* coordinate slightly increased with the application of the coating, indicating a small reduction in the blue hue intensity. The values of the overall color difference ΔE (Table 4) indicate that the TiO_2 coating had no effect on the aesthetic appearance of the specimen with $\Delta E < 1$, meaning not perceptible by human eyes. However, by adding other components, particularly γ-Fe_2O_3, ΔE values increased slightly, but still below 3, which means the color differences are perceptible only by close observation and are therefore more than acceptable.

3.3. Photoactivity under UV and Visible Lights.

The photocatalytic degradation of MB with TiO_2, rGO, TiO_2@Si, TiO_2@Si:Fe, and TiO_2@Si:Fe:rGO coated films under UV and visible lights was investigated (Figure 5). First, samples were immersed in the dye solution in dark: the equilibrium adsorption state was reached in 30 min, and MB adsorption on all of the samples was negligible. Degradation extents after 6 h UV irradiation were about 32% for pure TiO_2, 20% for pure rGO, 54% for TiO_2@Si, and more than 76% and 83% for TiO_2@Si:Fe and TiO_2@Si:Fe:rGO, respectively. These amounts decreased to about 9%, 8%, 32%, 54%, and 71% under visible light.

Results were plotted as ln C/C_0 versus time, obtaining linear trends with correlation coefficients (R^2) higher than 0.9 as expected in the pseudo-first-order kinetics model.[55,64] Kinetic constant (k) and band gaps of TiO_2, TiO_2@Si, TiO_2@Si:Fe, and TiO_2@Si:Fe:rGO coated films are reported in Table 5. The direct band gap values reported were determined by extrapolating the linear region of the Tauc's plot of $(\alpha h\upsilon)^{0.5}$ against photon energy, starting from absorbance data reported in Figure S3.

The increased efficiencies obtained in each addition of a compound to the sol are explained in the following. SiO_2 both increased the anatase content and reduced particle size, avoiding agglomeration. γ-Fe_2O_3 improved charge separation and reduced electron−hole recombination by receiving in its conduction band (CB) electrons photogenerated in TiO_2 and transferring holes photogenerated in its valence band (VB) to that of TiO_2. The incorporation of rGO into the composite led to band gap reduction. In fact, as shown in Figure S3 light absorption increased in the TiO_2@Si:Fe:rGO nanocomposite, suggesting that this sample could exhibit an enhanced photocatalytic activity. Moreover, photogenerated electrons can easily migrate to the rGO sheets, leading to effective separation and decreased recombination rate of photogenerated electron and hole pairs. In fact, the sheets of rGO can act as an excellent speed charge transfer channel to

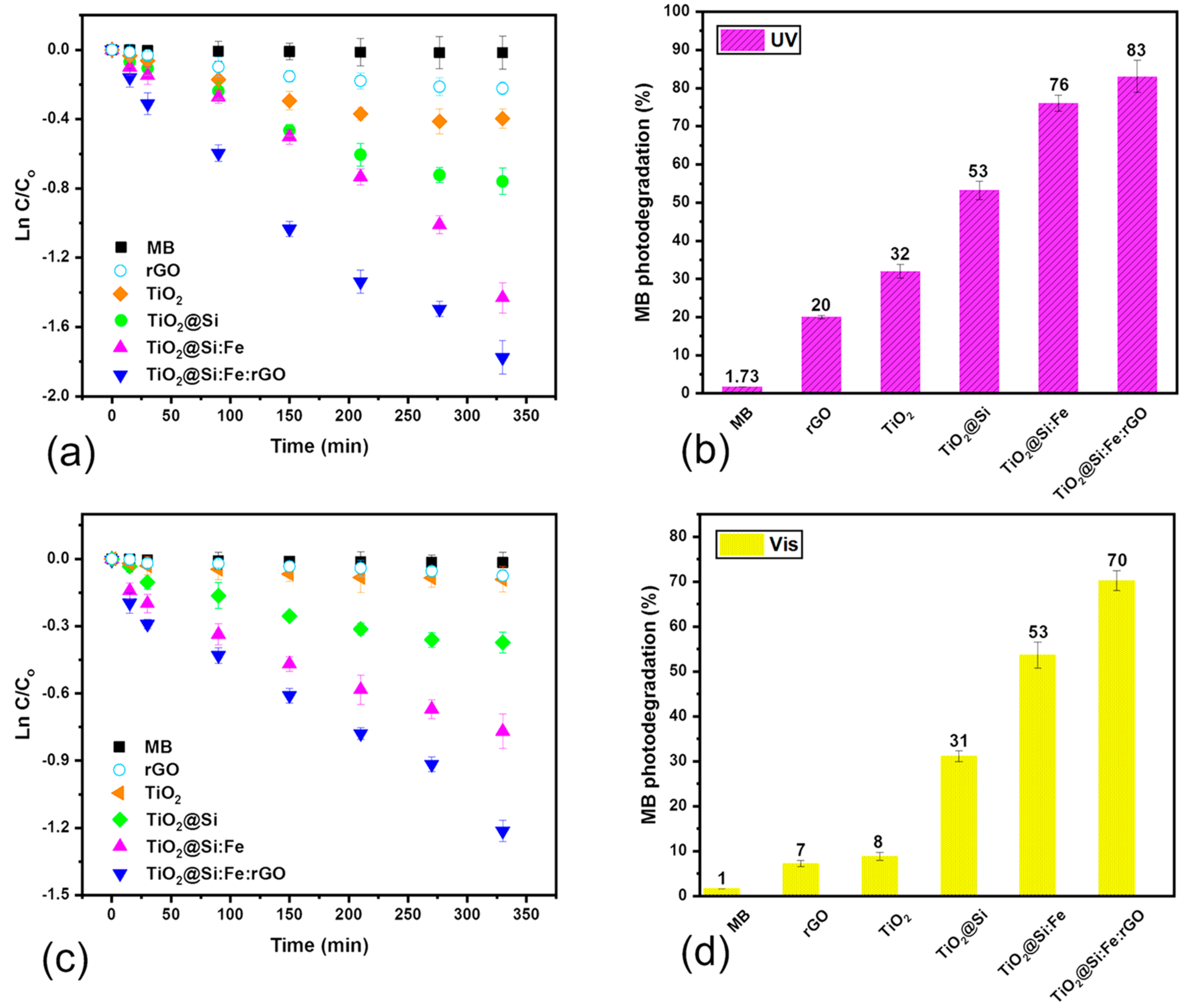

Figure 5. Photocatalytic activity for degradation of MB under (a,b) UV and (c,d) vis lights for MB, TiO_2, TiO_2@Si, TiO_2@Si:Fe, and TiO_2@Si:Fe:rGO coated films.

Table 5. Kinetic Constants of Photocatalytic MB Degradation under UV and Visible Light and Band Gaps of TiO_2, rGO, TiO_2@Si, TiO_2@Si:Fe, and TiO_2@Si:Fe:rGO Thin Films[a]

	UV		visible		
sample	K (min^{-1})	R^2	K (min^{-1})	R^2	band gap (eV)
MB	n/a	0.95	n/a	0.93	
rGO	n/a	0.94	n/a	0.95	
TiO_2	−0.0013	0.93	n/a	0.91	3.20
TiO_2@Si	−0.0024	0.98	−0.0012	0.94	3.03
TiO_2@Si:Fe	−0.0040	0.97	−0.0022	0.97	2.87
TiO_2@Si:Fe:rGO	−0.0053	0.98	−0.0032	0.98	2.26

[a] n/a = too low to be evaluated.

enhance the charge separation efficiency. Also, rGO sheets keep nanoparticles dispersed, preventing agglomeration.[68−71]

3.4. Evaluation of Coating Integrity. As mentioned above, mechanical durability and excellent adhesion of coatings could guarantee them undamaged in long-term use in cultural heritage field. We compared durability and surface structure of the TiO_2@Si:Fe:rGO and TiO_2 coated films by OM analysis (Figure 6). While TiO_2 presents several cracks on its surface, the TiO_2@Si:Fe:rGO coated film presents a uniform and dense structure without cracks. Surface structure was evaluated even after long-time immersion and photocatalysis tests. While the TiO_2@Si:Fe:rGO film remains unchanged during degradation tests, the amount of cracks in the TiO_2 coating increased significantly after exposure to the acid environment due to its weak stability.

Scratch test was performed as a destructive method to test the adhesion of such soft coatings deposited on hard substrates such as titanium[72] (Figure 6). As revealed by OM images, in the TiO_2 film, dense networks of lateral cracks could be observed alongside the scratch trail on the surface. These cracks are much more apparent compared to the TiO_2@Si:Fe:rGO film, with considerably fewer nucleation regions to cracking; in the latter case, by rubbing the scratched region with fingers, the scratched film was not easily removed.

Generally, the improvement in interfacial adhesion and mechanical stability could be related to better interactions

https://dx.doi.org/10.1021/acsami.0c06792
ACS Appl. Mater. Interfaces 2020, 12, 29671−29683

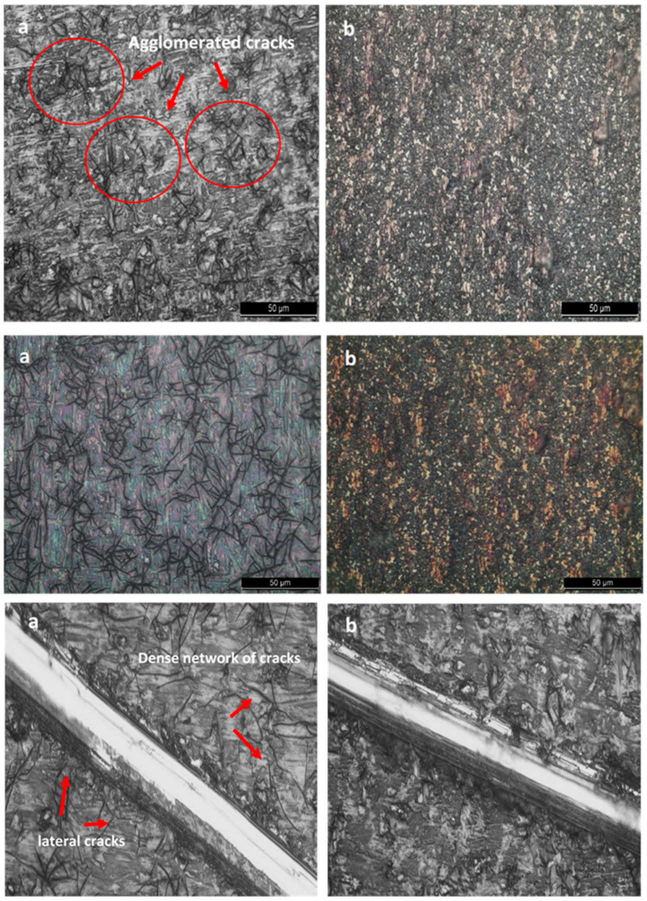

Figure 6. Optical microscopy images (500×) of newly deposited thin films (top), same coatings after acid rain test (middle), and scratched surfaces (bottom) (scale bars represent 25 μm): (a) TiO_2 and (b) TiO_2@Si:Fe:rGO films.

between the TiO_2@Si:Fe:rGO film and titanium surface. According to previous reports, the addition of SiO_2 and Fe_2O_3 to TiO_2 thin films could display very high adhesive and cohesive strengths in comparison with pure TiO_2 thin films.[73−78] Besides, the unique two-dimensional carbon-based structures such as GO (and rGO) sheets could act effectively at deflecting cracks at the metal/film interface, also improving coating density and adhesion through a multilayer structure.[79−84]

3.5. Self-Cleaning and Discoloration Resistance Tests.

Wettability, measured by water contact angle (CA), is a critical property in self-cleaning studies depending on the chemical composition and the morphology of the solid surfaces.[85−87] The surface wettability of the coated surfaces was investigated by measuring CA in the dark and after light irradiation for 30 min. The shape of the water droplet and CA values are given in Figure 7.

CA values measured before and after light irradiation show significant differences between coated substrates. In particular, water CA on TiO_2@Si coating decreases after exposure to light, probably due to SiO_2, which suppresses the transformation of anatase to rutile and the crystal growth of anatase (see Figure 2a,b). Furthermore, it favors water adsorption as shown by increased surface hydroxyl groups observed in FTIR characterization, which helps superhydrophilicity be maintained for an extended period.[88]

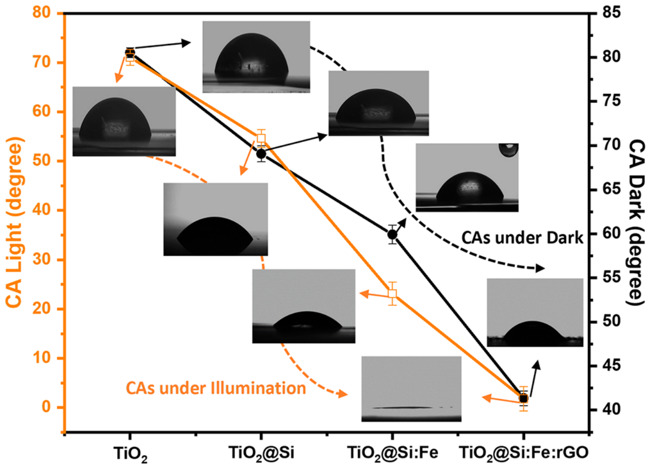

Figure 7. Evolution of water CA in dark and under illumination, with images of water CAs on TiO_2, TiO_2@Si, TiO_2@Si: Fe, and TiO_2@Si: Fe:rGO.

Clearly, by adding γ-Fe_2O_3 to TiO_2/SiO_2 structure, wettability under light irradiation further increased thanks to the improved charge separation and decreased recombination phenomena.[89] Indeed, the introduction of Fe^{3+} ions in TiO_2@Si:Fe film is responsible for a reduction in the photogenerated hole−electron recombination rate. Then, more photogenerated holes can oxidize the lattice O_2^- anions, creating more oxygen vacancies; eventually, water molecules may coordinate into the oxygen vacancy sites, leading to dissociative adsorption of water molecules on the surface, increasing surface hydroxyl content and reducing CA upon irradiation.[90]

The decrease in CA appeared much more abrupt by adding rGO, both in the dark and under light. Indeed, rGO had a major effect on wettability: after illumination, water CA changed clearly from hydrophilic (CA 41.3°) to superhydrophilic with CA < 2°. Furthermore, CA remained relatively constant even after turning off light and approached the initial dark state gradually.

The role of rGO on coating wettability could be attributed to the following mechanism. With the aid of UV irradiation, oxygen molecules on graphene are motivated from the ground spin-triplet state to a higher energy spin-singlet, resulting in electron−hole pairs which in turn form superoxide anions.[91,92] This leads to depletion of a large number of oxygen atoms, which in turn results in a continuous diffusion of oxygen vacancies on the rGO surface. Water molecules in air capture these vacancies to generate hydroxyl radicals, which bind to the carbon atom of the rGO in a supramolecular form (rather than in the form of a covalent bond) converting the hydrophilic TiO_2@Si:Fe:rGO composite (in the dark) into superhydrophilic TiO_2@Si:Fe:rGO under irradiation.[93,94] The adsorption of water molecules on the rGO defect surface further imparts it with superhydrophilicity. Under dark, these supramolecules gradually disappear on account of a lack of adequate energy supply.[94] Subsequently, oxygen molecules substitute for water molecules deposited on the graphene defect surface, which induces the return to hydrophilicity. If hydroxyl radicals were attached to the carbon atom of rGO by covalent bonds, they would not disappear in the absence of light. In the case of rGO, the hydroxyl groups are covalently bound to carbon atoms, so after a time in the dark storage, the rGO surface is not capable of converting into the initial CA immediately because of their presence. The following equations can be used to describe the reaction mechanisms:

$$\mathrm{rGO} + h\nu \rightarrow \mathrm{rGO(h^{+}{+}e^{-})} \quad (2)$$

$$\mathrm{e^{-}} + \mathrm{O_2} \rightarrow \mathrm{O_2}^{-\circ} \quad (3)$$

$$\mathrm{h^{+}} + \mathrm{OH^{-}} \rightarrow \mathrm{OH^{\circ}} \quad (4)$$

$$2\mathrm{O_2}^{-\circ} + 2\mathrm{H_2O} \rightarrow 2\mathrm{OH^{\circ}} + 2\mathrm{OH^{-}} + \mathrm{O_2} \quad (5)$$

In addition to the above discussions, transition in CA can be related to surface properties, primarily surface roughness. As a result, the droplet can spread on uneven surfaces formed after adding the components SiO_2, γ-Fe_2O_3, and rGO, as indicated by the increasing surface roughness (Figure 4), and thus enhancing hydrophilicity.[95,96]

Figure 8 shows the effect of different artificial acid rain solutions of pHs 3−7 on color differences and the amount of TiC (detected by XRD) on bare uncoated specimens after immersion for 7 days (also see Figures S4 and S5 and Table S1). As the pH fell to roughly 4.5 or below (acidic), color alteration, ΔE, increased rapidly, leading to discoloration comparable to that in the outdoor atmosphere. The color difference, ΔE, increased with immersion time, exceeding a value of 16 with an artificial acid rain of pH 3. However, in the pH 7 solution color variations were lower than 3, hence not noticeable.

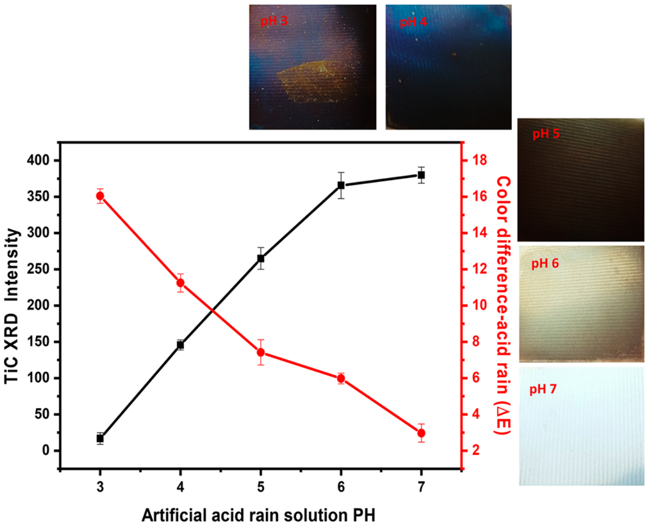

Figure 8. Effect of different pHs on the discoloration of titanium sheet and TiC XRD intensity (accelerated discoloration test: 65 °C, 7 days).

It is presumed that discoloration in the atmosphere is an interference color caused by the dissolution of titanium in acid rain, which forms TiO_2 on the sheet surfaces; the oxide film grows thicker, causing the interference color when thickness exceeds a few tens of nanometers.[4] The presence of TiC can also play a role in discoloration, as underlined by the following considerations. When discoloration accelerates markedly, the presence of TiC on the surfaces decreases significantly (see Figure 8). Indeed, TiC dissolves more than ten times more easily in a sulfuric acid solution than metallic titanium does.[37] The dissolved TiC quickly forms Ti ions, which then turn into TiO_2 through hydrolysis, depositing on the metal surface and increasing discoloration by interference as the oxide film grows.[37]

In contrast with other samples, at pH 4—where bare titanium already suffered from a heavy attack—in TiO_2@Si:Fe:rGO coated specimens, the color difference was less than 1 and not distinguishable by naked eyes, indicating that the coated film protects the substrate significantly with barrier effect (Figure 9).

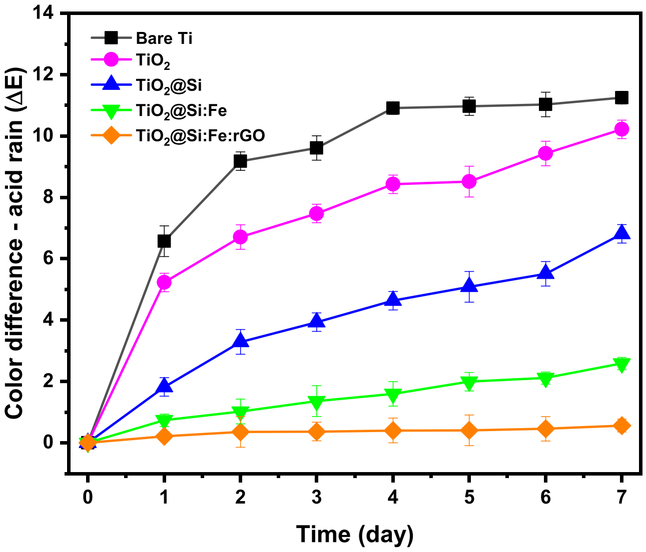

Figure 9. Discoloration test results of bare Ti and coated Ti with TiO_2, TiO_2@Si, TiO_2@Si:Fe, and TiO_2@Si:Fe:rGO sols in an acid solution of pH 4 at 65 °C.

Despite excellent discoloration resistance of the TiO_2@Si:Fe:rGO coated specimens (and considerably the TiO_2@Si:Fe film), other samples are susceptible to degradation at pH 4. Namely, the color difference of TiO_2 and TiO_2@Si sheets increased with immersion time in acid rain, reaching values of 7 and 10, respectively.

Furthermore, results in Figure S6 and Table S2 demonstrate that the wettability of the TiO_2@Si:Fe:rGO thin film is not affected significantly by the discoloration tests. Interestingly, the film not only could protect titanium from discoloration but also kept its own integrity against chemical or physical decomposition, which could result in crack formation. In contrast, TiO_2 wettability (as a comparison) showed an increase by about 10° to 15° both in dark and under illumination after discoloration. As the TiO_2 film could not prevent titanium from changing color, i.e., from oxidizing (see Figure 9), then the new oxide film growth may have damaged the sol−gel derived TiO_2 film.[97] Consequently, this led to a change in wettability, tending more to hydrophobicity.

Figure 10 shows the color difference developed in simulated soiling tests for uncoated and coated titanium specimens exposed to the five different soiling conditions simulating the different environments considered. As can be seen, the self-cleaning performance of the specimens depends on the type of pollutants, which are different on the basis of the place. As expected, all of the coated sheets show lower ΔE than the bare sheet, while coated films do not show similar behaviors. On the basis of the results, it can be discussed that TiO_2@Si:Fe:rGO coated film could act more efficiently rather than other films thanks to its significant self-cleaning properties. This result was

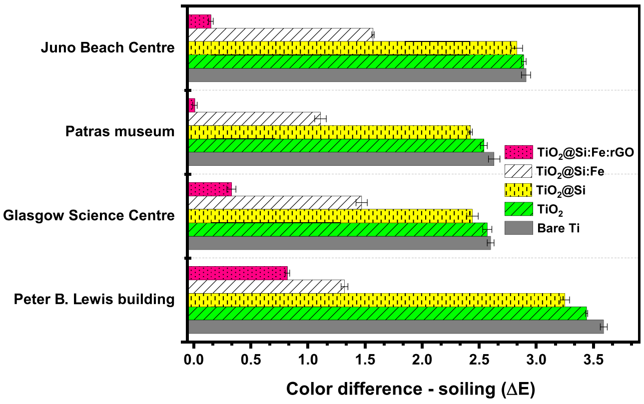

Figure 10. Color difference due to the simulated soiling test for the bare and coated titanium specimens exposed to soiling conditions simulating different places (June beach center (France), Patras museum (Greece), Glasgow science center (The U.K.), and Peter B Lewis building (USA)).

expected considering its superhydrophilicity and excellent photoactivity after illumination, as discussed above. Furthermore, results (Figure S7 and Table S3) confirm that the TiO_2@Si:Fe:rGO film could keep its appearance almost unchanged even after the soiling tests.

Soiling in real outdoor conditions was actually performed by exposing samples to the polluted atmosphere of Milan, Italy. Figure 11 shows ΔE values measured at the beginning of each month during the six months exposure. Moreover, the local average rainfall and sunlight irradiation index obtained from “air.plumelabs“ and “weather-atlas” databases during this period are indexed in the graph.

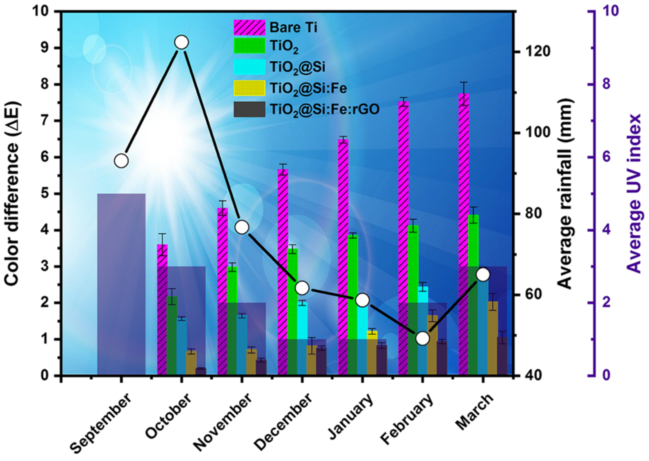

Figure 11. Color difference of the bare and coated titanium specimens exposed to the roof for 6 months (affected by average rainfall and UV index).

The high pollution concentration in September (41.2 μg/m^3) (Table 6) gave rise to an initial steep increase of ΔE values for all samples, coated and uncoated. As expected, bare titanium showed higher ΔE due to the lack of any protective self-cleaning layer on the surface. Interestingly, in the case of the TiO_2@Si and TiO_2@Si:Fe films, the coated layers preserved the titanium sheet by on setting self-cleaning conditions, benefiting from considerable rainfall and UV irradiation. Afterward, color-changing increased unfavorably, especially on bare titanium and TiO_2 coated substrates. In the case of TiO_2@Si and TiO_2@Si:Fe films, these changes were more significant compared to the contribution of the first month, due to low related rainfall and UV which decreased the chances of self-cleaning.

Table 6. Pollutant Concentration (μg/m^3) from September to March

	Sep	Oct	Nov	Dec	Jan	Feb	Mar
pollutant concn (μg/m^3)	41.2	19.5	23	16.5	50	49	18

The most noticeable results were obtained once again on the TiO_2@Si:Fe:rGO coated film after six months of exposure, with an overall ΔE lower than 1, meaning that the appearance did not show any color difference detectable by eye, meaning that it maintained self-cleaning properties also in a period of low rainfall and UV.

4. CONCLUSION

The fabricated transparent TiO_2@Si:Fe:rGO composite showed excellent photoactivity and wettability, behaving well in self-cleaning applications. Addition of SiO_2 improves the morphology, crystalline structure, and surface hydroxylation of TiO_2 nanoparticles and γ-Fe_2O_3 decreases the recombination rate of e^-/h^+ pairs and largely improves photocatalytic activity under visible light. Moreover, the rGO sheets also reduce recombination and improve nanoparticle dispersion. rGO also showed a significant effect on wettability, leading to a lower contact angle of the TiO_2@Si:Fe:rGO coated surface in dark and to superhydrophilicity under irradiation. On the basis of this study, the prepared TiO_2@Si:Fe:rGO composite coating is an efficient photocatalyst for degradation of contaminants under UV and visible light illumination and allows one to convert surface wettability to superhydrophilicity. Furthermore, the film revealed a proper adhesion integrity even after photodegradation tests, as well as superhydrophilicity even after discoloration tests.

Concerning the self-cleaning behavior, all coatings were sufficiently transparent to avoid alteration of the substrate color. Moreover, simulation of contact with acid rain caused negligible color change for TiO_2@Si:Fe:rGO coated surface. On the basis of simulated soiling tests, the same coating allowed efficient self-cleaning thanks to its significant superhydrophilicity and excellent photoactivity. These results were confirmed by roofing tests, where again negligible color changes were induced by atmospheric exposure of the coated samples. These results pave the way for potential use of the produced coating as a protective layer on metallic substrates working outdoors, such as in the built environment.

■ ASSOCIATED CONTENT

SI Supporting Information

The Supporting Information is available free of charge at https://pubs.acs.org/doi/10.1021/acsami.0c06792.

Synthesis schematic representation, artifacts photographs, samples’ absorbance spectra, discoloration photographs, samples’ color differences, XRD results, contact angle photographs, and photographs of samples after soiling tests (PDF)

AUTHOR INFORMATION

Corresponding Author

Maria Vittoria Diamanti − *Department of Chemistry, Materials and Chemical Engineering "Giulio Natta", Politecnico di Milano, Milan 20133, Italy;* orcid.org/0000-0003-4785-2473; Email: mariavittoria.diamanti@polimi.it

Authors

Maryam Mokhtarifar − *Department of Chemistry, Materials and Chemical Engineering "Giulio Natta", Politecnico di Milano, Milan 20133, Italy*

Reyhaneh Kaveh − *Department of Chemistry, Sharif University of Technology, Tehran 11365-11155, Iran*

Mojtaba Bagherzadeh − *Department of Chemistry, Sharif University of Technology, Tehran 11365-11155, Iran*

Andrea Lucotti − *Department of Chemistry, Materials and Chemical Engineering "Giulio Natta", Politecnico di Milano, Milan 20133, Italy*

MariaPia Pedeferri − *Department of Chemistry, Materials and Chemical Engineering "Giulio Natta", Politecnico di Milano, Milan 20133, Italy*

Complete contact information is available at: https://pubs.acs.org/10.1021/acsami.0c06792

Notes

The authors declare no competing financial interest.

ACKNOWLEDGMENTS

This work was supported by MIUR, Grant PRIN 2015WBEP3H "Monitoraggio, Consolidamento, Conservazione e Protezione di Beni Culturali".

REFERENCES

(1) Mokhtarifar, M.; Pedeferri, M. P.; Diamanti, M. V. Towards a Better Preservation of Current and Future Outdoor Architectural Heritage; Maximum Suppression of Discolouration in Anodized and Non-Anodized Titanium Sheets. *Environ. Technol. Rev.* **2020**, *9*, 37.

(2) Screpanti, A.; De Marco, A. Corrosion on Cultural Heritage Buildings in Italy: A Role for Ozone? *Environ. Pollut.* **2009**, *157* (5), 1513−1520.

(3) Bernard, M. C.; Joiret, S. Understanding Corrosion of Ancient Metals for the Conservation of Cultural Heritage. *Electrochim. Acta* **2009**, *54* (22), 5199−5205.

(4) Diamanti, M. V.; Aliverti, S.; Pedeferri, M. P. Decoupling the Dual Source of Colour Alteration of Architectural Titanium: Soiling or Oxidation? *Corros. Sci.* **2013**, *72*, 125−132.

(5) Goidanich, S.; Brunk, J.; Herting, G.; Arenas, M. A.; Odnevall Wallinder, I. Atmospheric Corrosion of Brass in Outdoor Applications. Patina Evolution, Metal Release and Aesthetic Appearance at Urban Exposure Conditions. *Sci. Total Environ.* **2011**, *412*−*413*, 46−57.

(6) Pelegrini, R. T.; Freire, R. S.; Duran, N.; Bertazzoli, R. Photoassisted Electrochemical Degradation of Organic Pollutants on a DSA Type Oxide Electrode: Process Test for a Phenol Synthetic Solution and Its Application for the E1 Bleach Kraft Mill Effluent. *Environ. Sci. Technol.* **2001**, *35* (13), 2849−2853.

(7) Vohra, M. S.; Tanaka, K. Photocatalytic Degradation of Aqueous Pollutants Using Silica-Modified TiO2. *Water Res.* **2003**, *37* (16), 3992−3996.

(8) Hepel, M.; Luo, J. Photoelectrochemical Mineralization of Textile Diazo Dye Pollutants Using Nanocrystalline WO3 Electrodes. *Electrochim. Acta* **2001**, *47* (5), 729−740.

(9) Pauporté, T.; Rathouský, J. Electrodeposited Mesoporous ZnO Thin Films as Efficient Photocatalysts for the Degradation of Dye Pollutants. *J. Phys. Chem. C* **2007**, *111* (21), 7639−7644.

(10) Paolini, R.; Borroni, D.; Pedeferri, M. P.; Diamanti, M. V. Self-Cleaning Building Materials: The Multifaceted Effects of Titanium Dioxide. *Constr. Build. Mater.* **2018**, *182*, 126−133.

(11) Diamanti, M. V.; Paolini, R.; Rossini, M.; Aslan, A. B.; Zinzi, M.; Poli, T.; Pedeferri, M. P. Long Term Self-Cleaning and Photocatalytic Performance of Anatase Added Mortars Exposed to the Urban Environment. *Constr. Build. Mater.* **2015**, *96*, 270−278.

(12) Puzenat, E.; Pichat, P. Studying TiO2 Coatings on Silica-Covered Glass by O2 Photosorption Measurements and FTIR-ATR Spectrometry: Correlation with the Self-Cleaning Efficacy. *J. Photochem. Photobiol., A* **2003**, *160* (1−2), 127−133.

(13) Kalousek, V.; Tschirch, J.; Bahnemann, D.; Rathouský, J. Mesoporous Layers of TiO2 as Highly Efficient Photocatalysts for the Purification of Air. *Superlattices Microstruct.* **2008**, *44* (4−5), 506−513.

(14) Zvonkina, I. J.; Hilt, M. Strategies for Developing Multi-Functional, Self-Healing Coatings for Corrosion Prevention and Other Functions. *In Handbook of Smart Coatings for Materials Protection* **2014**, 105−120.

(15) Banerjee, S.; Pillai, S. C.; Falaras, P.; O'shea, K. E.; Byrne, J. A.; Dionysiou, D. D. New Insights into the Mechanism of Visible Light Photocatalysis. *J. Phys. Chem. Lett.* **2014**, *5* (15), 2543−2554.

(16) Nguyen, P. T. N.; Salim, C.; Kurniawan, W.; Hinode, H. A Non-Hydrolytic Sol-Gel Synthesis of Reduced Graphene Oxide/TiO 2 Microsphere Photocatalysts. *Catal. Today* **2014**, *230*, 166−173.

(17) Rezaei, M.; Salem, S. Photocatalytic Activity Enhancement of Anatase-Graphene Nanocomposite for Methylene Removal: Degradation and Kinetics. *Spectrochim. Acta, Part A* **2016**, *167*, 41−49.

(18) Kwon, C. H.; Kim, J. H.; Jung, I. S.; Shin, H.; Yoon, K. H. Preparation and Characterization of TiO2-SiO2 Nano-Composite Thin Films. *Ceram. Int.* **2003**, *29*, 851.

(19) Sun, S.; Deng, T.; Ding, H.; Chen, Y.; Chen, W. Preparation of Nano-TiO2-Coated SiO2Microsphere Composite Material and Evaluation of Its Self-Cleaning Property. *Nanomaterials* **2017**, *7*, 367.

(20) Dai, X.; Lu, G.; Hu, Y.; Xie, X.; Wang, X.; Sun, J. Reversible Redox Behavior of Fe 2 O 3 /TiO 2 Composites in the Gaseous Photodegradation Process. *Ceram. Int.* **2019**, *45*, 13187.

(21) Alsharaeh, E. H.; Bora, T.; Soliman, A.; Ahmed, F.; Bharath, G.; Ghoniem, M. G.; Abu-Salah, K. M.; Dutta, J. Sol-Gel-Assisted Microwave-Derived Synthesis of Anatase Ag/Tio2/Go Nanohybrids toward Efficient Visible Light Phenol Degradation. *Catalysts* **2017**, *7*, 133.

(22) Weinstein, S. J.; Ruschak, K. J. Dip Coating on a Planar Non-Vertical Substrate in the Limit of Negligible Surface Tension. *Chem. Eng. Sci.* **2001**, *56*, 4957.

(23) Hu, Z.; Zhang, J.; Xiong, S.; Zhao, Y. Annealing-Free, Air-Processed and High-Efficiency Polymer Solar Cells Fabricated by a Dip Coating Process. *Org. Electron.* **2012**, *13*, 142.

(24) Rajabi, N.; Heshmatpour, F.; Malekfar, R.; Bahari-Poor, H. R.; Abyar, S. A Comparative Study of Dip Coating and Spray Pyrolysis Methods for Synthesizing ITO Nanolayers by Using Ag Colloidal Sol. *Mater. Sci.-Pol.* **2014**, *32*, 102.

(25) Grosso, D. How to Exploit the Full Potential of the Dip-Coating Process to Better Control Film Formation. *J. Mater. Chem.* **2011**, *21*, 17033.

(26) Faustini, M.; Louis, B.; Albouy, P. A.; Kuemmel, M.; Grosso, D. Preparation of Sol-Gel Films by Dip-Coating in Extreme Conditions. *J. Phys. Chem. C* **2010**, *114*, 7637.

(27) Guglielmi, M.; Colombo, P.; Peron, F.; Mancinelli Degli Esposti, L. Dependence of Thickness on the Withdrawal Speed for SiO2 and TiO2 Coatings Obtained by the Dipping Method. *J. Mater. Sci.* **1992**, *27*, 5052.

(28) Ceratti, D. R.; Louis, B.; Paquez, X.; Faustini, M.; Grosso, D. A New Dip Coating Method to Obtain Large-Surface Coatings with a Minimum of Solution. *Adv. Mater.* **2015**, *27*, 4958.

(29) Bottein, T.; Loizillon, J.; Grosso, D. Full Investigation of Angle Dependence in Dip-Coating Sol-Gel Films. *J. Phys. Chem. B* **2017**, *121*, 6220.

(30) Spurr, R. A.; Myers, H. Quantitative Analysis of Anatase-Rutile Mixtures with an X-Ray Diffractometer. *Anal. Chem.* **1957**, *29* (5), 760−762.

(31) Murphy, A. B. Band-Gap Determination from Diffuse Reflectance Measurements of Semiconductor Films, and Application to Photoelectrochemical Water-Splitting. *Sol. Energy Mater. Sol. Cells* **2007**, *91* (14), 1326−1337.

(32) Bagherzadeh, M.; Kaveh, R. A New SnS2-BiFeO3/Reduced Graphene Oxide Photocatalyst with Superior Photocatalytic Capability under Visible Light Irradiation. *J. Photochem. Photobiol., A* **2018**, *359*, 11−22.

(33) Bagherzadeh, M.; Kaveh, R.; Ozkar, S.; Akbayrak, S. Preparation and Characterization of a New CdS−NiFe2O4/Reduced Graphene Oxide Photocatalyst and Its Use for Degradation of Methylene Blue under Visible Light Irradiation. *Res. Chem. Intermed.* **2018**, *44* (10), 5953−5979.

(34) Jacobson, M. Z. Climate Response of Fossil Fuel and Biofuel Soot, Accounting for Soot's Feedback to Snow and Sea Ice Albedo and Emissivity. *J. Geophys. Res. D Atmos.* **2004**, *109*, D21.

(35) Sleiman, M.; Kirchstetter, T. W.; Berdahl, P.; Gilbert, H. E.; Quelen, S.; Marlot, L.; Preble, C. V.; Chen, S.; Montalbano, A.; Rosseler, O.; Akbari, H.; Levinson, R.; Destaillats, H. Soiling of Building Envelope Surfaces and Its Effect on Solar Reflectance - Part II: Development of an Accelerated Aging Method for Roofing Materials. *Sol. Energy Mater. Sol. Cells* **2014**, *122*, 271−281.

(36) Favez, O.; Cachier, H.; Chabas, A.; Ausset, P.; Lefevre, R. Crossed Optical and Chemical Evaluations of Modern Glass Soiling in Various European Urban Environments. *Atmos. Environ.* **2006**, *40* (37), 7192−7204.

(37) Kaneko, M.; Takahashi, K.; Hayashi, T.; Muto, I.; Tokuno, K.; Kimura, K. Environmental and Metallurgical Factors Affecting Discoloration of Titanium Sheets in Atmospheric Environments. *Tetsu to Hagane* **2003**, *89* (8), 833−840.

(38) Hikosaka, T.; Mizutani, N.; Tanaka, Y.; Hoshiai, K.; Hasegawa, N.; Muraji, N.; Hirai, H.; Ohta, I.; Kawai, T.; Tsuruta, S. Studies on Discoloration and Electrochemical Corrosion of Titanium and Titanium Alloys. *Nihon Hotetsu Shika Gakkai Zasshi* **2003**, *47* (2), 301−310.

(39) Kaneko, M.; Kimura, M.; Tokuno, K. Effects of Titanium Carbide (TiC) and Anodizing Voltages on Discoloration Resistance of Colored-Titanium Sheets. *Corros. Sci.* **2010**, *52* (6), 1889−1896.

(40) Takahashi, K.; Kaneko, M.; Hayashi, T.; Muto, I.; Tamenari, J.; Tokuno, K. Improvement of Discoloration Resistance of Vacuum Annealed Commercially Pure Titanium Sheets in Atmospheric Environments. *Tetsu to Hagane* **2004**, *90* (5), 278−285.

(41) Kaneko, M.; Takahashi, K.; Hayashi, T.; Tokuno, K.; Tamenari, J. Discoloration Resistance of Architectural Titanium Sheets in Long-Term Atmospheric Exposure Tests. *Mater. Perform.* **2006**, 38.

(42) Mahyar, A.; Behnajady, M. A.; Modirshahla, N. Characterization and Photocatalytic Activity of SiO2-TiO2 Mixed Oxide Nanoparticles Prepared by Sol-Gel Method. *Indian J. Chem., Sect. A: Inorg., Bio-inorg., Phys., Theor. Anal. Chem.* **2010**, *49* (12), 1593.

(43) Gribb, A. A.; Banfield, J. F. Particle Size Effects on Transformation Kinetics and Phase Stability in Nanocrystalline TiO2. *Am. Mineral.* **1997**, *82*, 717.

(44) Zhang, H.; Chen, B.; Banfield, J. F. The Size Dependence of the Surface Free Energy of Titania Nanocrystals. *Phys. Chem. Chem. Phys.* **2009**, *11*, 2553.

(45) Chang, H.; Kim, S. K.; Jang, H. D.; Cho, S. W. Effect of SiO2 Nanoparticles on the Phase Transformation of TiO2 in Micron-Sized Porous TiO2-SiO2 Mixed Particles. *Mater. Lett.* **2011**, *65*, 3272.

(46) Ghorai, T. K.; Chakraborty, M.; Pramanik, P. Photocatalytic Performance of Nano-Photocatalyst from TiO2 and Fe2O3 by Mechanochemical Synthesis. *J. Alloys Compd.* **2011**, *509* (32), 8158−8164.

(47) Hung, W. H.; Chien, T. M.; Tseng, C. M. Enhanced Photocatalytic Water Splitting by Plasmonic TiO 2-Fe2O3 Cocatalyst under Visible Light Irradiation. *J. Phys. Chem. C* **2014**, *118* (24), 12676−12681.

(48) Abbas, N.; Shao, G. N.; Haider, M. S.; Imran, S. M.; Park, S. S.; Kim, H. T. Sol−Gel Synthesis of TiO2-Fe2O3 Systems: Effects of Fe2O3 Content and Their Photocatalytic Properties. *J. Ind. Eng. Chem.* **2016**, *39*, 112−120.

(49) Tobaldi, D. M.; Pullar, R. C.; Gualtieri, A. F.; Seabra, M. P.; Labrincha, J. A. Sol-Gel Synthesis, Characterisation and Photocatalytic Activity of Pure, W-, Ag- and W/Ag Co-Doped TiO2 Nanopowders. *Chem. Eng. J.* **2013**, *214*, 364−375.

(50) Xu, Y. J.; Zhuang, Y.; Fu, X. New Insight for Enhanced Photocatalytic Activity of TiO2 by Doping Carbon Nanotubes: A Case Study on Degradation of Benzene and Methyl Orange. *J. Phys. Chem. C* **2010**, *114* (6), 2669−2676.

(51) Xiong, Z.; Wu, H.; Zhang, L.; Gu, Y.; Zhao, X. S. Synthesis of TiO2 with Controllable Ratio of Anatase to Rutile. *J. Mater. Chem. A* **2014**, *2* (24), 9291−9297.

(52) Cheng, H.; Ma, J.; Zhao, Z.; Qi, L. Hydrothermal Preparation of Uniform Nanosize Rutile and Anatase Particles. *Chem. Mater.* **1995**, *7* (4), 663−671.

(53) Wang, D.; Li, X.; Chen, J.; Tao, X. Enhanced Photoelectrocatalytic Activity of Reduced Graphene Oxide/TiO 2 Composite Films for Dye Degradation. *Chem. Eng. J.* **2012**, *198*−*199*, 547−554.

(54) Sher Shah, M. S. A.; Park, A. R.; Zhang, K.; Park, J. H.; Yoo, P. J. Green Synthesis of Biphasic TiO 2-Reduced Graphene Oxide Nanocomposites with Highly Enhanced Photocatalytic Activity. *ACS Appl. Mater. Interfaces* **2012**, *4* (8), 3893−3901.

(55) Mohamed, H. H. Biphasic TiO2Microspheres/Reduced Graphene Oxide for Effective Simultaneous Photocatalytic Reduction and Oxidation Processes. *Appl. Catal., A* **2017**, *541*, 25−34.

(56) Li, G.; Lan, J.; Li, G. Chrysanthemum-like 3D Hierarchical Magnetic γ-Fe2O3 and Fe3O4 Superstructures: Facile Synthesis and Application in Adsorption of Organic Pollutants from Water. *RSC Adv.* **2015**, *5* (3), 1705−1711.

(57) Huang, C. H.; Bai, H.; Liu, S. L.; Huang, Y. L.; Tseng, Y. H. Synthesis of Neutral SiO2/TiO2 Hydrosol and Its Photocatalytic Degradation of Nitric Oxide Gas. *Micro Nano Lett.* **2011**, *6* (8), 646−649.

(58) Gao, X.; Wachs, I. E. Titania-Silica as Catalysts: Molecular Structural Characteristics and Physico-Chemical Properties. *Catal. Today* **1999**, *51* (2), 233−254.

(59) Pal, B.; Hata, T.; Goto, K.; Nogami, G. Photocatalytic Degradation of O-Cresol Sensitized by Iron-Titania Binary Photocatalysts. *J. Mol. Catal. A: Chem.* **2001**, *169*, 147.

(60) Botelho, G.; Andres, J.; Gracia, L.; Matos, L. S.; Longo, E. Photoluminescence and Photocatalytic Properties of Ag3PO4Microcrystals: An Experimental and Theoretical Investigation. *ChemPlusChem* **2016**, *81*, 202.

(61) Bagherzadeh, M.; Kaveh, R. New Magnetically Recyclable Reduced Graphene Oxide RGO/MFe2O4 (M = Ca, Mg)/Ag3PO4 Nanocomposites With Remarkably Enhanced Visible-Light Photocatalytic Activity and Stability. *Photochem. Photobiol.* **2018**, *94*, 1210.

(62) Daryaei, E.; Reza Rahimi Tabar, M.; Moshfegh, A. Z. Surface Roughness Analysis of Hydrophilic SiO2/TiO 2/Glass Nano Bilayers by the Level Crossing Approach. *Phys. A* **2013**, *392* (9), 2175−2181.

(63) Dhoke, S. K.; Khanna, A. S. Electrochemical Behavior of Nano-Iron Oxide Modified Alkyd Based Waterborne Coatings. *Mater. Chem. Phys.* **2009**, *117* (2−3), 550−556.

(64) Wei, Y.; Zhang, Y.; Gao, X.; Ma, Z.; Wang, X.; Gao, C. Multilayered Graphene Oxide Membrane for Water Treatment: A Review. *Carbon* **2018**, *139*, 964−981.

(65) Tsou, C. H.; An, Q. F.; Lo, S. C.; De Guzman, M.; Hung, W. S.; Hu, C. C.; Lee, K. R.; Lai, J. Y. Effect of Microstructure of Graphene Oxide Fabricated through Different Self-Assembly Techniques on 1-Butanol Dehydration. *J. Membr. Sci.* **2015**, *477*, 93−100.

(66) Hosseini, M.; Hamdy Makhlouf, A. S. *Industrial Applications for Intelligent Polymers and Coatings*; Springer: Cham, Switzerland, 2016. DOI: 10.1007/978-3-319-26893-4.

(67) Husain, A. A. F.; Hasan, W. Z. W.; Shafie, S.; Hamidon, M. N.; Pandey, S. S. A Review of Transparent Solar Photovoltaic Technologies. *Renewable Sustainable Energy Rev.* **2018**, *94*, 779−791.

(68) Wen, X.; Zhao, S.; Asuha, S. Preparation of Nitrogen-Doped Mesoporous Tio2/Rgo Composites and Its Application to Visible Light-Assisted Photocatalytic Degradation. *J. Nanomater.* **2019**, *2019*, 1.

(69) Liu, Y. Hydrothermal Synthesis of TiO2-RGO Composites and Their Improved Photocatalytic Activity in Visible Light. *RSC Adv.* **2014**, *4*, 36040.

(70) Tan, L.-L.; Ong, W.-J.; Chai, S.-P.; Mohamed, A. Reduced Graphene Oxide-TiO2 Nanocomposite as a Promising Visible-Light-Active Photocatalyst for the Conversion of Carbon Dioxide. *Nanoscale Res. Lett.* **2013**, *8*, 465.

(71) Hu, X. S.; Shen, Y.; Zhang, Y. T.; Nie, J. J. Preparation of Flower-like CuS/Reduced Graphene Oxide(RGO) Photocatalysts for Enhanced Photocatalytic Activity. *J. Phys. Chem. Solids* **2017**, *103*, 201.

(72) Bull, S. J.; Berasetegui, E. G. An Overview of the Potential of Quantitative Coating Adhesion Measurement by Scratch Testing. *Tribol. Int.* **2006**, *39*, 99.

(73) Jia, Q.; Zhang, Y.; Wu, Z.; Zhang, P. Tribological Properties of Anatase TiO 2 Sol-Gel Films Controlled by Mutually Soluble Dopants. *Tribol. Lett.* **2007**, *26*, 19.

(74) Chun, H. D.; Kim, J. S.; Yoon, S. M.; Kim, C. G. Physical Properties and Photocatalytic Performance of TiO2 Coated Stainless Steel Plate. *Korean J. Chem. Eng.* **2001**, *18*, 908.

(75) Dam Le, D.; Dung Dang, T. M.; Thang Chau, V.; Chien Dang, M. The Fabrication of Visible Light Responsive Ag-SiO2 Co-doped TiO2 Thin Films by the Sol-Gel Method. *Adv. Nat. Sci.: Nanosci. Nanotechnol.* **2010**, *1*, 015007.

(76) Li, Z.; Hou, B.; Xu, Y.; Wu, D.; Sun, Y.; Hu, W.; Deng, F. Comparative Study of Sol-Gel-Hydrothermal and Sol-Gel Synthesis of Titania-Silica Composite Nanoparticles. *J. Solid State Chem.* **2005**, *178*, 1395.

(77) Momeni, M.; Golestani-Fard, F.; Saghafian, H.; Barati, N.; Khanahmadi, A. Development of Visible Light Activated TiO 2 Thin Films on Stainless Steel via Sol Spraying with Emphasis on Microstructural Evolution and Photocatalytic Activity. *Appl. Surf. Sci.* **2015**, *357*, 1902.

(78) Momeni, M.; Saghafian, H.; Golestani-Fard, F.; Barati, N.; Khanahmadi, A. Effect of SiO2 Addition on Photocatalytic Activity, Water Contact Angle and Mechanical Stability of Visible Light Activated TiO2 Thin Films Applied on Stainless Steel by a Sol Gel Method. *Appl. Surf. Sci.* **2017**, *392*, 80.

(79) Zhang, X.; Fan, X.; Yan, C.; Li, H.; Zhu, Y.; Li, X.; Yu, L. Interfacial Microstructure and Properties of Carbon Fiber Composites Modified with Graphene Oxide. *ACS Appl. Mater. Interfaces* **2012**, *4*, 1543.

(80) Da, S. X.; Wang, J.; Geng, H. Z.; Jia, S. L.; Xu, C. X.; Li, L. G.; Shi, P. P.; Li, G. High Adhesion Transparent Conducting Films Using Graphene Oxide Hybrid Carbon Nanotubes. *Appl. Surf. Sci.* **2017**, *392*, 1117.

(81) Lu, H.; Yao, Y.; Huang, W. M.; Hui, D. Noncovalently Functionalized Carbon Fiber by Grafted Self-Assembled Graphene Oxide and the Synergistic Effect on Polymeric Shape Memory Nanocomposites. *Composites, Part B* **2014**, *67*, 290.

(82) Ning, H.; Li, J.; Hu, N.; Yan, C.; Liu, Y.; Wu, L.; Liu, F.; Zhang, J. Interlaminar Mechanical Properties of Carbon Fiber Reinforced Plastic Laminates Modified with Graphene Oxide Interleaf. *Carbon* **2015**, *91*, 224.

(83) Son, G. C.; Hwang, D. K.; Jang, J.; Chee, S. S.; Cho, K.; Myoung, J. M.; Ham, M. H. Solution-Processed Highly Adhesive Graphene Coatings for Corrosion Inhibition of Metals. *Nano Res.* **2019**, *12*, 19.

(84) Moon, I. K.; Kim, J. Il; Lee, H.; Hur, K.; Kim, W. C.; Lee, H. 2D Graphene Oxide Nanosheets as an Adhesive Over-Coating Layer for Flexible Transparent Conductive Electrodes. *Sci. Rep.* **2013**, *3*, 1112.

(85) Wang, J.; Zhang, Y.; Wang, S.; Song, Y.; Jiang, L. Bioinspired Colloidal Photonic Crystals with Controllable Wettability. *Acc. Chem. Res.* **2011**, *44* (6), 405−415.

(86) Wang, J.; Wen, Y.; Hu, J.; Song, Y.; Jiang, L. Fine Control of the Wettability Transition Temperature of Colloidal-Crystal Films: From Superhydrophilic to Superhydrophobic. *Adv. Funct. Mater.* **2007**, *17* (2), 219−225.

(87) Li, Q.; Guo, Z. Lubricant-Infused Slippery Surfaces: Facile Fabrication, Unique Liquid Repellence and Antireflective Properties. *J. Colloid Interface Sci.* **2019**, *536*, 507−515.

(88) Huang, T.; Huang, W.; Zhou, C.; Situ, Y.; Huang, H. Superhydrophilicity of TiO2/SiO2 Thin Films: Synergistic Effect of SiO2 and Phase-Separation-Induced Porous Structure. *Surf. Coat. Technol.* **2012**, *213*, 126−132.

(89) Yu, J. C.; Ho, W.; Lin, J.; Yip, H.; Wong, P. K. Photocatalytic Activity, Antibacterial Effect, and Photoinduced Hydrophilicity of TiO2 Films Coated on a Stainless Steel Substrate. *Environ. Sci. Technol.* **2003**, *37* (10), 2296−2301.

(90) Yu, J.; Zhou, M.; Yu, H.; Zhang, Q.; Yu, Y. Enhanced Photoinduced Super-Hydrophilicity of the Sol-Gel-Derived TiO 2 Thin Films by Fe-Doping. *Mater. Chem. Phys.* **2006**, *95* (2−3), 193−196.

(91) Feng, X.; Zhai, J.; Jiang, L. The Fabrication and Switchable Superhydrophobicity of TiO2 Nanorod Films. *Angew. Chem., Int. Ed.* **2005**, *44* (32), 5115−5118.

(92) Kim, S. B.; Hwang, H. T.; Hong, S. C. Photocatalytic Degradation of Volatile Organic Compounds at the Gas-Solid Interface of a TiO2 Photocatalyst. *Chemosphere* **2002**, *48* (4), 437−444.

(93) Luo, Z.; Pinto, N. J.; Davila, Y.; Charlie Johnson, A. T. Controlled Doping of Graphene Using Ultraviolet Irradiation. *Appl. Phys. Lett.* **2012**, *100* (25), 253108.

(94) Duong, D. L.; Han, G. H.; Lee, S. M.; Gunes, F.; Kim, E. S.; Kim, S. T.; Kim, H.; Ta, Q. H.; So, K. P.; Yoon, S. J.; Chae, S. J.; Jo, Y. W.; Park, M. H.; Chae, S. H.; Lim, S. C.; Choi, J. Y.; Lee, Y. H. Probing Graphene Grain Boundaries with Optical Microscopy. *Nature* **2012**, *490* (7419), 235−239.

(95) Bharti, B.; Kumar, S.; Kumar, R. Superhydrophilic TiO 2 Thin Film by Nanometer Scale Surface Roughness and Dangling Bonds. *Appl. Surf. Sci.* **2016**, *364*, 51−60.

(96) Wang, R.; Hashimoto, K.; Fujishima, A.; Chikuni, M.; Kojima, E.; Kitamura, A.; Shimohigoshi, M.; Watanabe, T. Light-Induced Amphiphilic Surfaces [4]. *Nature* **1997**, *388*, 431−432.

(97) Maeda, H.; Kobayashi, T.; Konishi, S. Patterning of Wettability Using the Photocatalytic Decomposition of Hydrophobic Self-Assembled Monolayer on the TiO2 Pattern. *Jpn. J. Appl. Phys.* **2017**, *56*, 06GN09.